buildings

MDPI

Article

Dosage-Dependent Regulation of β-Hemihydrate Phosphogypsum by Calcium Sulfate Whiskers: Workability, Dry–Wet Strength and Pore Structure

Siqing Cao [1], Han Zhou [1,*], Tianci Lu [1], Zhirui Zhang [1], Yi Xu [1], Jiawei Jiao [2] and Dongxu Li [2]

[1] School of Urban Science and Offshore Engineering, Nantong Institute of Technology, Nantong 226001, China; 2510310018@ntit.edu.cn (Y.X.)
[2] College of Material Science and Engineering, Nanjing Tech University, Nanjing 211800, China
* Correspondence: 20246260@ntit.edu.cn

Abstract

The use of β-hemihydrate phosphogypsum (β-HPG) in building materials is limited by insufficient strength and water sensitivity. This study evaluated calcium sulfate whiskers (CSW) as a modifier at 0–4 wt% relative to β-HPG mass under a fixed water-to-gypsum ratio of 0.58. Workability, dry flexural and compressive strengths, wet compressive strength, and water resistance were assessed alongside isothermal calorimetry, X-ray diffraction, mercury intrusion porosimetry, and scanning electron microscopy. The 2 wt% mixture showed the highest mean dry flexural and compressive strengths among the tested formulations, reaching 5.95 and 22.0 MPa, respectively, approximately 49% and 23% higher than the control. Wet compressive strength after 24 h immersion increased from 7.4 to approximately 8.5 MPa at this dosage. The corresponding paste spread diameter was 155 mm. Higher dosages further reduced mercury-accessible porosity and water absorption without exceeding these mean strengths. The higher wet strengths were accompanied by lower softening-coefficient estimates. CSW advanced the hydration heat-flow peak, while dihydrate gypsum remained the dominant crystalline phase. This integrated assessment distinguishes pore-volume reduction from mechanical improvement and absolute wet strength from relative strength retention. The findings provide an experimental basis for selecting CSW-modified phosphogypsum formulations according to strength, workability, and moisture-exposure requirements.

Keywords: β-hemihydrate phosphogypsum; calcium sulfate whisker; hydration heat evolution; pore structure; micromorphology

Check for updates

Academic Editor: Ahmet Benli

Received: 7 September 2026
Revised: 20 September 2026
Accepted: 25 September 2026
Published: 29 September 2026

Copyright: © 2026 by the authors. Licensee MDPI, Basel, Switzerland. This article is an open access article distributed under the terms and conditions of the Creative Commons Attribution (CC BY) license.

1. Introduction

Industrial by-products can replace conventional raw materials and modify binder reactions and hardened microstructure. Recent studies have examined recovered cement paste in clinker production [1], waste glass and steel slag in mortar [2], recycled powders in alkali-activated slag concrete [3], and iron-mining waste in fired bricks [4]. Research on fly ash- and slag-containing concrete also relates moisture-dependent hydration and pore characteristics to strength and freeze–thaw resistance [5]. In gypsum binders, Kamarou et al. [6] reported improved strength and water-resistance coefficients using waste-derived additives. These studies motivate the development of phosphogypsum-based binders that combine resource utilization with suitable mechanical and moisture-related performance. Phosphogypsum is an important example of an industrial by-product with potential for use

as a construction binder. Pretreatment and calcination can convert it into β-hemihydrate phosphogypsum (β-HPG), which can be used in gypsum-based building products [7–9]. However, obtaining adequate workability often requires more water than is consumed by hydration. The excess water can leave pores after drying and thereby weaken the hardened skeleton. Huang et al. [10] demonstrated the importance of water-content regulation in phosphorus building gypsum, while Chen et al. [11] compared phosphogypsum-, natural-gypsum-, and flue-gas-desulfurization (FGD) gypsum-derived hemihydrates and documented differences in their material characteristics. The resulting differences in water demand, crystal packing, and pore structure are important when evaluating the dry and wet mechanical performance of β-HPG [10–12].

Several modification strategies have been developed for gypsum-based materials, including mineral additions, polymers, water-reducing agents, surface treatments, and fiber reinforcement [13–18]. One-dimensional reinforcement can improve resistance to cracking, but its effects depend on the matrix and interface. Numerical research on fiber-assisted carbonate precipitation in cement stone further links fiber geometry and mineral deposition to strength and permeability [19]. Recent phosphogypsum research also shows the importance of balancing different performance requirements. Zhang et al. [20] developed fiber-reinforced foamed phosphogypsum composites and examined the effects of foaming, fiber incorporation, and foam stabilization. Increased foaming improved thermal insulation and acoustic absorption but reduced mechanical strength and water resistance. Fiber incorporation, particularly PVA fiber, helped improve the latter properties. Their results demonstrate the need to evaluate mechanical improvement together with water-related performance in reinforced phosphogypsum materials.

Calcium sulfate whiskers (CSW) are of interest because they combine a needle-like or rod-like morphology with a calcium sulfate composition. Their one-dimensional geometry offers potential for connecting crystal clusters and interacting with developing cracks. Their composition provides a basis for compatibility with the gypsum matrix [21–23]. Wang et al. [21] investigated modified calcium sulfate hemihydrate whiskers in gypsum composites and examined their effects on physical properties, mechanical performance, and microstructure. Jian et al. [22] studied whisker-modified FGD gypsum and discussed the associated performance and structural changes. Related work has also explored the production of whiskers from FGD gypsum for binder modification [24,25]. These findings support examining CSW dosage in relation to the characteristics of the β-HPG matrix and its hardened structure. Jiao et al. [26] investigated the combined activation of multiphase phosphogypsum using sodium sulfate and CSW. Unlike that combined-activation system, the present study examines a graded CSW addition series in a β-HPG matrix. Wang et al. [27] evaluated strain-hardening gypsum composites under normal, dry, and saturated conditions and found that polyethylene fibers enhanced tensile deformation capacity without improving water resistance. Building on these studies, the present work examines whether the dosage associated with the greatest strength also provides the lowest water uptake and the highest relative strength retention in β-HPG.

The central question is whether continued reduction in mercury-accessible porosity produces a corresponding increase in dry and wet strength. A second question is whether higher absolute wet strength is accompanied by greater relative strength retention, as distinguished by the softening coefficient [6,27]. Addressing both questions within one dosage series provides a basis for selecting formulations according to their intended performance requirements. This study therefore investigated commercial CSW as a modifier for β-HPG at dosages of 0–4 wt% relative to the mass of β-HPG. The water-to-gypsum ratio (W/G ratio) was fixed at 0.58. Paste fluidity and setting time were evaluated together with dry flexural strength, dry and wet compressive strengths, water absorption, and softening coef-

ficient. Isothermal calorimetry, qualitative X-ray diffraction, mercury intrusion porosimetry, and scanning electron microscopy were used to examine the associated hydration and microstructural responses. The study relates dosage-dependent changes in workability, early heat evolution, crystalline phases, accessible pore structure, and dry–wet strength. Its contribution is to distinguish strength-oriented and pore-related formulation outcomes in CSW-modified β-HPG.

2. Materials and Methods

2.1. Materials

The raw β-HPG was obtained from Shandong Xinfa Group Co., Ltd. (Liaocheng, Shandong, China). Its phase composition and particle size distribution are shown in Figure 1. Figure 1a shows that $CaSO_4 \cdot 0.5H_2O$ is the main crystalline phase. A small amount of SiO_2 is also present as an impurity phase. Figure 1b shows a broad particle size distribution. The basic physical and mechanical properties of β-HPG are listed in Table 1, and its chemical composition is presented in Table 2.

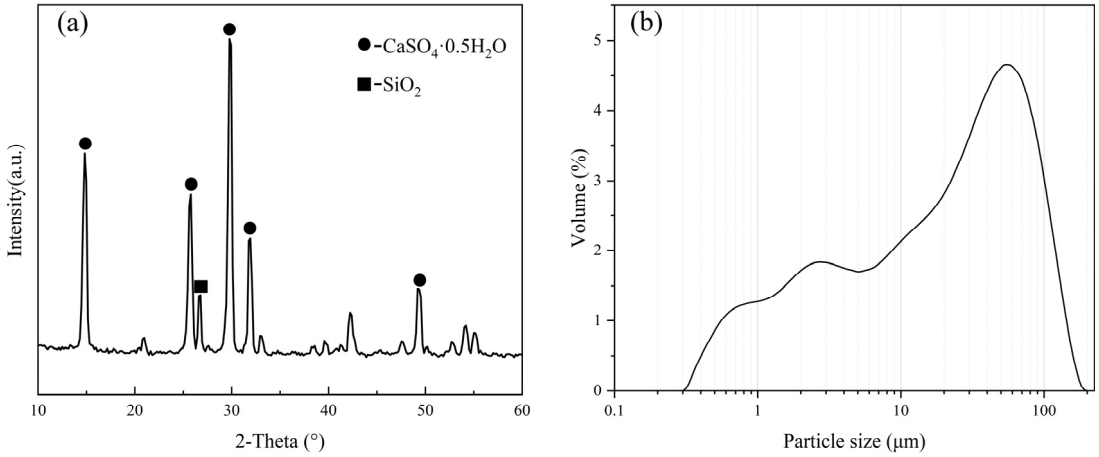


Figure 1. (**a**) XRD pattern and (**b**) particle size distribution of β-HPG.

Table 1. Physical and mechanical properties of β-HPG.

Standard Water Content for Uniform Consistency (%)	Setting Time (min)		Flexural Strength (MPa)		Compressive Strength (MPa)	
	Initial Setting	Final Setting	2 h	7 d-Dry	2 h	7 d-Dry
58.0	18	21	3.94	3.97	6.94	17.90

Table 2. Chemical composition of β-HPG.

Component	SO_3	CaO	SiO_2	Al_2O_3	P_2O_5	K_2O	Fe_2O_3	MgO	TiO_2	LOI
Content (wt %)	46.19	32.71	8.15	1.20	1.06	0.51	0.48	0.36	0.14	8.99

Calcium sulfate whisker (CSW) was purchased from Shanghai Fengzhu New Materials Co., Ltd. (Shanghai, China). under the model designation NP-S02. The selected CSW was a white fibrous powder. Its macroscopic appearance, micromorphology, and phase composition are shown in Figure 2. According to the SEM image in Figure 2b, the CSW mainly exhibited elongated columnar, needle-like, or rod-like morphology. The whiskers had relatively intact crystal shapes and a high aspect ratio. The physical properties of CSW are listed in Table 3. It should be noted that the tensile strength and elastic modulus listed in Table 3 are nominal values provided by the manufacturer for individual calcium sulfate

whiskers. They were not measured in this study. These values were used only to describe the intrinsic high-strength and high-modulus characteristics of CSW as a one-dimensional reinforcing material. They were not used for quantitative mechanical modeling or strength prediction. The diameter, aspect ratio, pH, and purity were also taken from the supplier's product information. Figure 2c identifies anhydrous $CaSO_4$ as the predominant starting phase of CSW. Its potential hydration to gypsum [28,29] is considered when interpreting the composite calorimetric response in Section 3.4.

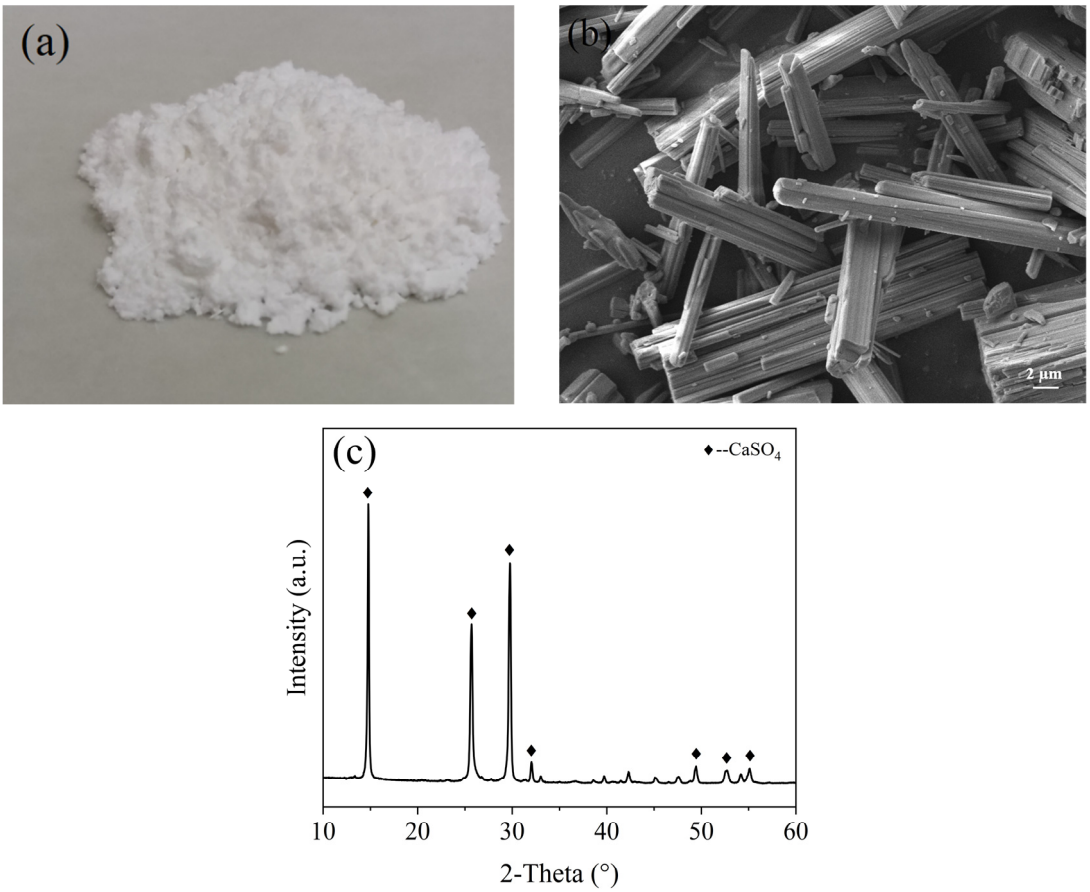


Figure 2. Characteristics of CSW: (**a**) visual appearance; (**b**) SEM micrograph; (**c**) XRD pattern.

Table 3. Manufacturer-reported physical properties of calcium sulfate whiskers.

Model	Diameter (μm)	Length-to-Diameter Ratio	pH	Tensile Strength (GPa)	Elastic Modulus (GPa)	Purity (%)
NP-S02	1–4	10–40	7	20	170	98

2.2. Experimental Methods

All mixtures contained the same mass of β-HPG powder. CSW was added at 0, 1, 2, 3, and 4 wt% relative to the β-HPG mass, while the W/G ratio was fixed at 0.58. The experimental flowchart for specimen preparation was shown in Figure 3. For each formulation, the constituent powders were weighed according to the designed mass proportions. The weighed powders were placed in a plastic airtight bag and dry-mixed for 5 min before paste preparation. CSW was incorporated into the powder blend during this dry-premixing step. The purpose of premixing was to distribute the added powder within the β-HPG. The

water-to-total-solid mass ratio (W/S ratio) was defined using the combined initial masses of β-HPG and CSW:

$$\frac{W}{S} = \frac{m_W}{m_G + m_{CSW}} = \frac{0.58}{1 + d} \quad (1)$$

where $d = m_{CSW}/m_G$. The calculated W/S ratio therefore decreased from 0.580 for C-0 to 0.558 for C-4. The water added per unit mass of β-HPG remained unchanged. The decrease in W/S ratio arose from the additional solid mass and was not a measured decrease in free water. The mixtures were not adjusted to a constant W/S ratio or matched fluidity. The experimental series consequently evaluates the combined response to CSW addition under a fixed-W/G design, rather than independently isolating whisker reinforcement from water-ratio and workability effects.

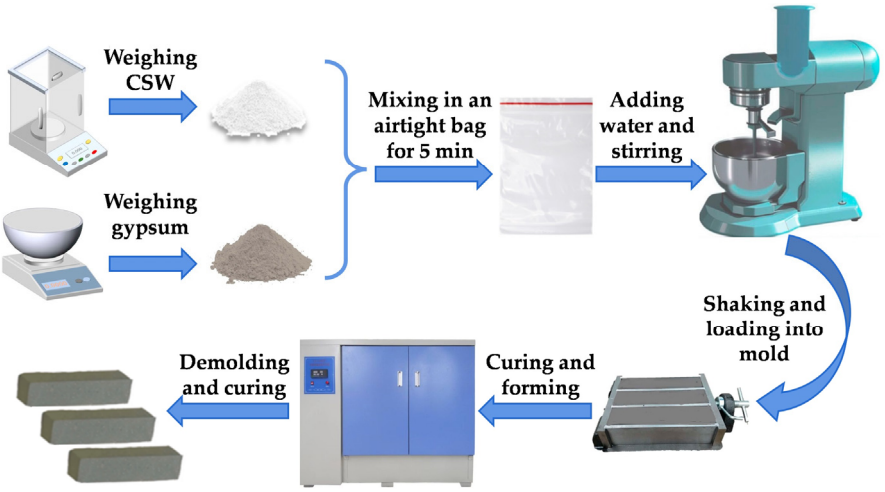


Figure 3. Experimental flowchart for specimen preparation.

The mechanical strengths of the specimens were measured according to the Calcined Gypsum (GB/T 9776-2022) [30]. After curing for 7 d, the specimens were dried in an oven at 45 ± 2 °C to constant mass. Three flexural strength tests were conducted for each mixture. After the flexural test, the broken halves were used for compressive strength testing, and six compressive strength values were obtained for each mixture. The average values were reported as the dry flexural and dry compressive strengths.

The wet compressive strength was measured to evaluate the load-bearing capacity of β-HPG after water exposure. The dried specimens were immersed in water at 20 ± 2 °C for 24 h. After immersion, the surface water was gently removed using a wet cloth, and the compressive strength was measured immediately. Six wet compressive strength values were obtained for each mixture. The softening coefficient was calculated using Equation (2):

$$K = \frac{f_w}{f_d}, \quad (2)$$

where K is the softening coefficient, f_w is the wet compressive strength after 24 h of water immersion, and f_d is the dry compressive strength of specimens with the same mix proportion.

Water absorption was also used to evaluate the water resistance of the hardened specimens. The specimens were dried to constant mass and then immersed in water at 20 ± 2 °C for 24 h. The water absorption was calculated using Equation (3):

$$W = \frac{m_w - m_d}{m_d} \times 100\%, \quad (3)$$

where W is the water absorption, m_d is the dry mass of the specimen, and m_w is the mass of the specimen after water immersion.

The fluidity of fresh β-HPG paste was assessed using a spread-diameter test based on the consistency-testing procedure referenced in the Gypsum Plasters—Determination of Physical Properties of Pure Paste (GB/T 17669.4–1999) [31]. The pastes were prepared according to the proportions listed in Table 4. Timing started when the β-HPG powder first came into contact with water. At 50 s, the mould of the consistency apparatus was lifted at a constant speed. The resulting paste spread was measured in two perpendicular directions, and the arithmetic mean of the two diameters was recorded as the paste fluidity. The initial setting time was defined as the time at which the Vicat needle penetrated the paste without touching the glass base plate. The final setting time was defined as the time at which the penetration depth of the needle from the surface was 0.5 mm.

Table 4. Normalized initial mixture proportions and calculated mass ratios.

Designation	β-HPG (wt%)	CSW (wt%)	W/G Ratio	Calculated Initial W/S Ratio
C-0	100.0	0	0.58	0.580
C-1	100.0	1.0	0.58	0.574
C-2	100.0	2.0	0.58	0.569
C-3	100.0	3.0	0.58	0.563
C-4	100.0	4.0	0.58	0.558

Early-age hydration heat evolution of the gypsum pastes was measured using a TAM Air 8 isothermal calorimeter (TA Instruments, New Castle, DE, USA). Each calorimetric specimen contained 4.00 g of initial total solids, comprising β-HPG and CSW. Both the specific heat-flow rate and cumulative heat release were normalized by this combined solid mass, excluding mixing water. The CSW dosage was expressed relative to β-HPG mass, whereas the calorimetric results were expressed per gram of the initial combined powder. The hardened gypsum specimens were thoroughly ground and dried, and their phase compositions were determined using a SmartLab™ X-ray diffractometer (Rigaku Corporation, Tokyo, Japan). The scanning rate was 10 °/min, and the scanning range was 10–60°. Hardened and dried specimens with dimensions of approximately 5 mm × 5 mm × 5 mm were attached to conductive adhesive tape and sputter-coated with gold to ensure electrical conductivity. The microstructure of the specimens was then observed using a JEOL IT-300 scanning electron microscope (JEOL Ltd., Tokyo, Japan). Mercury intrusion porosimetry was performed using a PoreMaster GT-6.0 porosimeter (Quantachrome Instruments, Boynton Beach, FL, USA), and the pore size distribution and porosity of the specimens were analyzed using PoreMaster software (Porowin-32).

3. Results and Discussion

3.1. Effect of CSW on the Workability of β-HPG

Figure 4 compares the paste spread diameters and setting times of the five β-HPG–CSW formulations at W/G = 0.58. As shown in Figure 4a, the C-0 paste showed a fluidity of 180 mm. With increasing CSW dosage, the paste fluidity decreased continuously. The fluidity values of C-1, C-2, C-3, and C-4 decreased to 168, 155, 138, and 110 mm, respectively. Compared with C-0, the corresponding fluidity losses were 6.7%, 13.9%, 23.3%, and 38.9%, respectively. The larger fluidity losses at 3 and 4 wt% indicate that increasing CSW dosage was accompanied by a greater reduction in paste spread under the investigated mixture conditions. The setting behavior showed a similar dosage-dependent response. As shown in Figure 4b, the initial and final setting times of C-0 were 18.9 min and 22.8 min, respectively.

After CSW incorporation, both the initial and final setting times decreased gradually. For C-4, the initial and final setting times decreased to 13.8 min and 16.7 min, corresponding to reductions of 27.0% and 26.8%, respectively. The CSW-containing pastes therefore reached the measured setting endpoints earlier. The combination of reduced spread and earlier setting highlights the need to consider the available working time when selecting the CSW dosage.

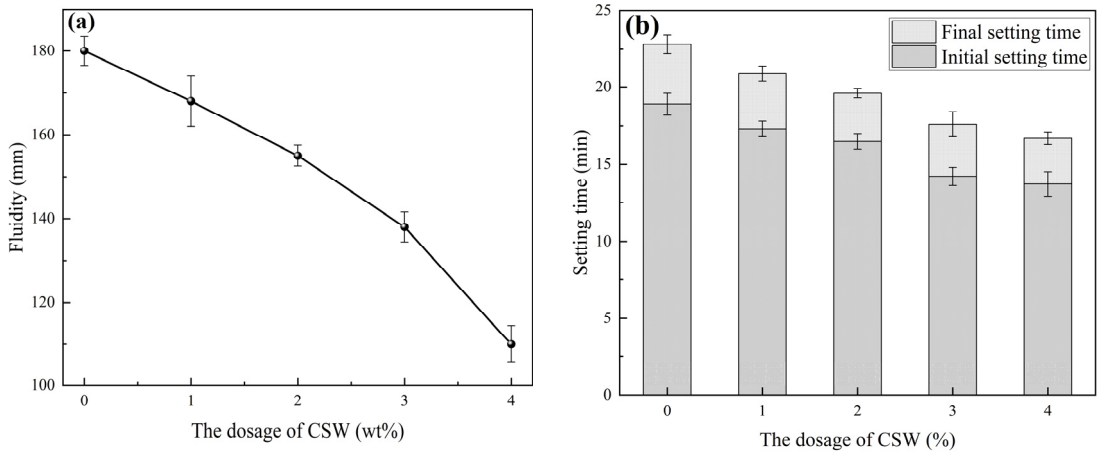


Figure 4. Effect of CSW on the (**a**) fluidity and (**b**) setting time of β-HPG paste.

As shown in Table 4, CSW addition reduced the initial W/S ratio while the water added per unit β-HPG mass remained constant. Water content and preparation conditions influence the flow response of gypsum binders [10,12]. The additional powder and its elongated geometry may also affect particle interactions and early structure formation. The measured spread therefore reflects the combined formulation change rather than a direct measurement of water adsorption. The shorter setting times may similarly involve changes in both reaction behavior and physical structure formation. A possible contribution from surface-assisted gypsum precipitation is discussed in Section 3.4. Such precipitation could contribute to earlier structural development, but its role remains a proposed explanation rather than direct evidence of heterogeneous nucleation on CSW surfaces. From a mixture-design perspective, the workability results should be considered alongside the intended mechanical performance. C-2 retained a spread diameter of 155 mm, compared with 138 and 110 mm for C-3 and C-4. Together with the shorter setting times at higher dosages, this difference identifies the workability trade-off to be considered alongside the strength results.

3.2. Effect of CSW on the Mechanical Properties of β-HPG

The effect of CSW on the dry mechanical properties of β-HPG is shown in Figure 5. The reported mean flexural and compressive strengths increased up to 2 wt% CSW and then decreased at higher dosages. All CSW-containing formulations nevertheless retained higher reported mean strengths than C-0. As shown in Figure 5a, the flexural strength of C-0 was 4.0 MPa. After the incorporation of 1 wt% CSW, the flexural strength increased to 5.4 MPa. When the CSW dosage increased to 2 wt%, the flexural strength reached the highest reported mean value of 5.95 MPa, corresponding to an increase of approximately 49% compared with C-0. When the CSW dosage was further increased to 3 wt% and 4 wt%, the flexural strength decreased to 5.8 MPa and 5.5 MPa, respectively. These results highlight the flexural-strength benefit of CSW addition, while showing that a higher dosage did not necessarily produce a greater strength gain. The compressive strength showed a similar trend, as shown in Figure 5b. The compressive strength of C-0 was 17.9 MPa. The value

increased with CSW incorporation and reached 22.0 MPa for C-2, which was approximately 23% higher than that of C-0. When the CSW dosage increased to 3 wt% and 4 wt%, the compressive strength decreased to 20.8 MPa. The strength ranking refers to the measured means; statistical separation of neighboring dosage groups was not established.

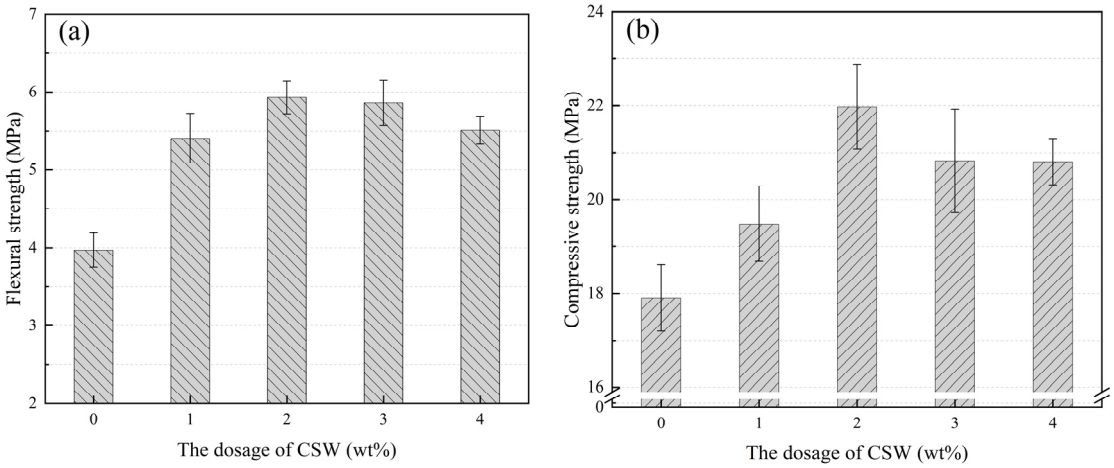


Figure 5. Effect of CSW on the (**a**) flexural strength and (**b**) compressive strength of β-HPG.

The strength gains were obtained under a fixed W/G ratio of 0.58. From C-0 to C-2, the W/S ratio decreased from 0.580 to 0.569, and fluidity decreased from 180 to 155 mm. Water content, specimen consolidation, and crystal packing are relevant to gypsum strength development [10,12]. Because W/S ratio and fluidity varied together with CSW addition, the measured gains represent the overall response of the formulations. The larger relative increase in flexural strength than in compressive strength is compatible with a possible reinforcing contribution from CSW. Previous studies on fiber- and whisker-modified gypsum have discussed crack bridging and interfacial energy dissipation as mechanisms that can improve resistance to bending failure [16,17,21,22]. These mechanisms provide a basis for interpreting the larger flexural-strength response in the present series. Whisker bridging and related interfacial processes are therefore considered possible contributions to the measured improvement.

The lower strengths at higher dosages may be associated with changes in local structural uniformity as well as the pronounced loss of fluidity. The more closely associated crystalline arrangement observed in C-2 and the localized bundles in C-4 provide morphological context for their different strength responses (Section 3.7). Local structural uniformity and fresh-paste behavior may contribute alongside accessible porosity, without assigning the strength difference exclusively to CSW agglomeration. Among the tested formulations, C-2 combined the highest mean dry strengths with greater paste spread than C-3 and C-4. This comparison identifies a promising tested dosage under W/G = 0.58, rather than an optimum between the discrete dosage levels.

3.3. Effect of CSW on the Water Resistance and Wet Strength of β-HPG

Figure 6 compares 24 h water absorption, wet compressive strength, and the softening coefficient. These measurements distinguish water uptake, absolute load-bearing capacity after immersion, and relative strength retention [15,27]. As shown in Figure 6a, the water absorption of β-HPG generally decreased with increasing CSW dosage. The water absorption of C-0 was 26.8%. After the incorporation of 1, 2, 3, and 4 wt% CSW, the water absorption decreased to 25.2%, 24.9%, 24.4%, and 24.3%, respectively. Compared with C-0, the reduction in water absorption reached 9.3% for C-4. This result indicates that CSW reduced the water uptake of hardened β-HPG. C-2 reduced water absorption by

approximately 7.1% relative to C-0. The lower water absorption accompanied a decrease in mercury-accessible porosity and a redistribution of mercury-accessible pore-entry sizes, as discussed in Section 3.6. These observations associate the absorption response with changes in accessible pore structure.

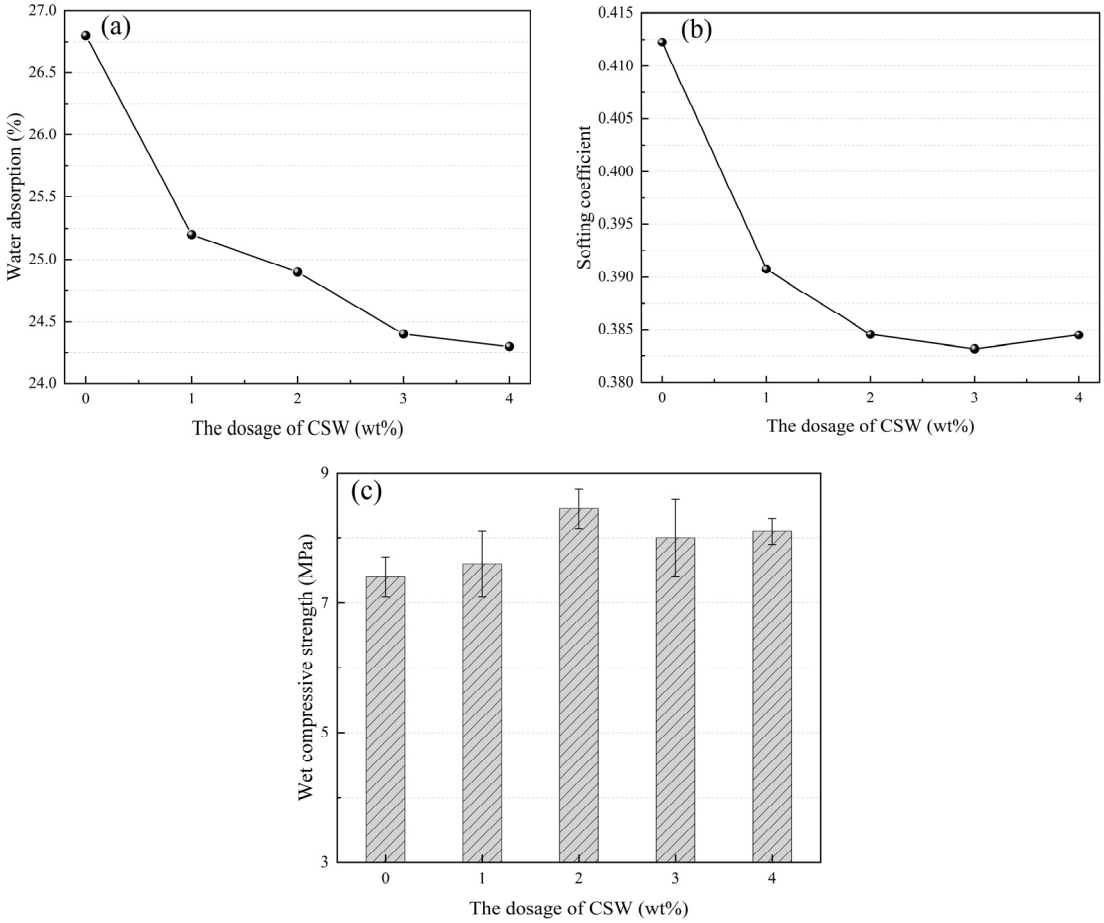


Figure 6. Effect of CSW on the water resistance and wet strength of β-HPG: (**a**) water absorption, (**b**) softening coefficient, and (**c**) wet compressive strength after 24 h of water immersion.

The wet compressive strength results are shown in Figure 6c. The wet compressive strength of C-0 was 7.4 MPa. After CSW incorporation, the wet compressive strength increased to different degrees. C-1 showed a wet compressive strength of 7.6 MPa, while C-2 reached the highest reported mean value of approximately 8.5 MPa. The wet compressive strengths of C-3 and C-4 were 8.0 and 8.1 MPa, respectively. The increase for C-2 was approximately 14.9% relative to C-0, showing that its mechanical benefit extended to the tested immersion condition. The highest mean dry and wet compressive strengths occurred in the same formulation, supporting C-2 as a promising tested composition for increasing absolute load-bearing capacity under both conditions.

The reported softening coefficient was 0.412 for C-0 and lower for the CSW-containing formulations (Figure 6b). For C-2, the proportional increase in dry compressive strength exceeded that in wet compressive strength, so the ratio decreased despite the higher absolute wet strength. This distinction is consistent with the separate evaluation of reinforcement and water resistance in previous gypsum research [27]. The small differences among C-2–C-4 require uncertainty estimates incorporating both strengths and are not treated as a statistically established ranking of water stability.

The water-resistance behavior should be interpreted from both pore structure and interfacial stability. The strength of the gypsum matrix depends on crystal contacts and

interlocking [32], while water-induced changes at these contacts provide a possible explanation for the difference between dry and wet performance [33]. Lower water uptake and preservation of load transfer during immersion are therefore complementary material-design objectives, rather than equivalent outcomes. The more closely associated crystalline arrangement observed in C-2 (Section 3.7) is consistent with its higher mean wet strength. C-4 showed the lowest measured water absorption, whereas C-2 combined a wet compressive strength of approximately 8.5 MPa with a water absorption of 24.9% and greater paste spread than C-3 and C-4. Under the fixed W/G ratio of 0.58, this combination favors C-2 when dry and wet load-bearing capacity are the principal formulation objectives. Relative strength retention remains a separate criterion: the reported softening-coefficient estimates did not show an improvement, and the small differences among neighboring dosage groups should be evaluated with uncertainty from both strength measurements.

3.4. Effect of CSW on the Hydration Heat Evolution of β-HPG

Figure 7 presents the heat-flow rates and cumulative heat releases of the β-HPG–CSW pastes during the first 480 min. Both quantities are normalized by the initial total solid mass, including β-HPG and CSW but excluding mixing water. All pastes exhibited a dominant exothermic peak, followed by a gradual decline in heat-flow rate. This profile is consistent with the dissolution–precipitation process of calcium sulfate hemihydrate hydration [34,35]. Hemihydrate dissolution supplies ions to the liquid phase, while dihydrate gypsum precipitates and grows as the solution becomes supersaturated. The heat-flow and cumulative-heat curves describe the timing, magnitude, and progression of this early calorimetric response. As shown in Figure 7a, the main peak of C-0 occurred at 23.0 min, with a heat-flow rate of 49.53 mW/g. The peaks of C-1 and C-2 occurred at 20.5 and 18.5 min, with corresponding values of 55.02 and 58.46 mW/g, respectively. C-2 showed the highest recorded peak, approximately 18.0% above C-0. For C-3 and C-4, the peaks occurred at 15.5 and 16.5 min, with values of 51.12 and 55.46 mW/g, respectively. All CSW-containing pastes therefore reached their main exothermic peaks earlier than C-0. C-2 combined earlier peak occurrence with the greatest peak heat-flow rate, whereas C-3 and C-4 reached their peaks sooner. These results distinguish the dosage associated with the earliest exothermic response from that associated with the highest peak magnitude.

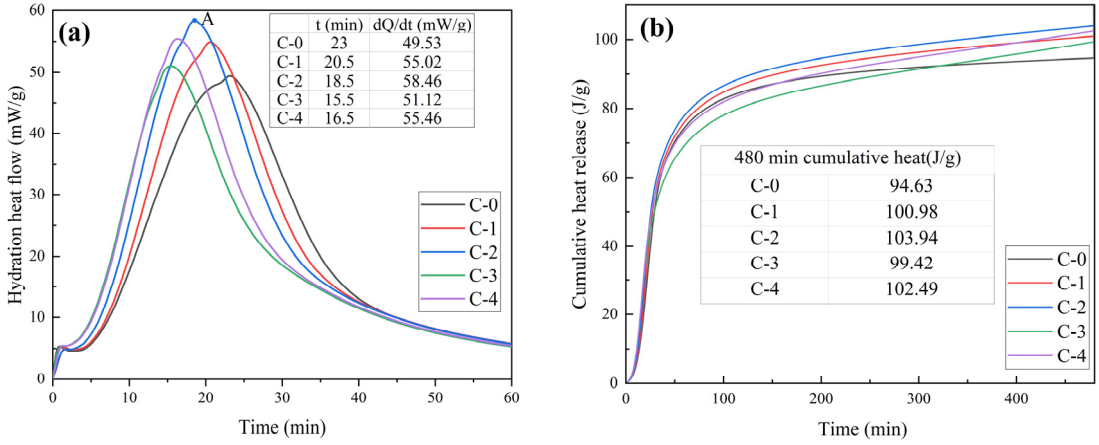


Figure 7. Effect of CSW on the early hydration heat evolution of β-HPG: (**a**) hydration heat-flow rate and (**b**) cumulative heat release within 480 min.

The cumulative heat curves in Figure 7b rose rapidly during the early measurement period and subsequently increased more slowly. At 480 min, the cumulative heat releases of C-0, C-1, C-2, C-3, and C-4 were 94.63, 100.98, 103.94, 99.42, and 102.50 J/g, respectively. C-2 showed the highest value, approximately 9.83% above C-0. All CSW-containing pastes thus

recorded higher cumulative heat than C-0 at 480 min, with C-2 exhibiting both the highest peak heat-flow rate and the greatest accumulated heat. The cumulative curves also reveal differences in the temporal distribution of heat release. At 60 min, C-3 and C-4 had released 69.26 and 73.59 J/g, respectively, compared with 74.44 J/g for C-0. Their cumulative values nevertheless exceeded those of C-0 by the end of the measurement. During 400–480 min, C-3 and C-4 released an additional 3.64 and 3.40 J/g, respectively, compared with 1.00 J/g for C-0. These larger later-stage contributions helped increase the cumulative heat of the higher-dosage formulations relative to the control. The results therefore show two distinct features of CSW modification: advancement of the main exothermic peak and redistribution of heat release over the subsequent period. The cumulative curves continued to rise toward 480 min, indicating that measurable heat evolution persisted at the selected endpoint.

The earlier peaks may involve additional surfaces for gypsum precipitation and the possible reaction of initially anhydrous CSW. CSW surfaces may provide additional interfaces associated with gypsum precipitation, which could contribute to the earlier exothermic response. This surface-associated effect is considered possible nucleation promotion rather than directly demonstrated heterogeneous nucleation. In addition, the starting CSW was identified as predominantly anhydrous $CaSO_4$. Anhydrous calcium sulfate can hydrate to $CaSO_4 \cdot 2H_2O$ under suitable aqueous conditions, including through dissolution and precipitation [36]. The added CSW may therefore participate both as a surface for precipitation and as a potentially reactive calcium sulfate constituent. Changes in the liquid–solid environment may also influence the resulting heat-release profile. Calorimetry records the complete formulation on a total-solid-mass basis and does not separate the heat contributions of β-HPG and CSW. The higher cumulative heat therefore cannot be assigned exclusively to β-HPG conversion, nor can the later heat release of C-3 and C-4 be assigned specifically to delayed CSW hydration. C-2 recorded the highest peak and cumulative heat within 480 min; later-age phase composition is examined separately in Section 3.5.

3.5. Effect of CSW on the Crystalline Phase Assemblage of β-HPG

XRD was used to identify the crystalline phases in the β-HPG specimens after 7 d of curing. Figure 8a shows broadly similar diffraction patterns across the investigated CSW dosages. Reflections at approximately 11.6°, 20.7°, and 29.1° were assigned to $CaSO_4 \cdot 2H_2O$, indicating that gypsum dominated the observed diffraction patterns. The reflection near 26.6° was assigned to SiO_2, which was also identified in the starting β-HPG. Phase identification was based on the combination of reflections across the measured range, rather than on the intensity of the 11.6° reflection alone. The raw β-HPG was dominated by hemihydrate, whereas the 7 d patterns were dominated by gypsum. No additional crystalline reaction product was confidently identified in the CSW-containing specimens relative to C-0. Any hydration of anhydrous CSW would contribute to the same gypsum phase [36], so similar product assemblages do not imply that the added whiskers remained chemically unchanged. Anhydrite and gypsum have distinct diffraction patterns [34], but the present qualitative analysis does not quantify residual anhydrite or apportion gypsum formation between the β-HPG and CSW precursors.

Figure 8b provides an enlarged view of the reflection between 11.3° and 11.9°. Differences in recorded intensity are visible among the specimens. Gypsum diffraction intensities can be influenced by crystal habit and preferred orientation, while powder preparation and packing can introduce additional variability [37,38]. Accordingly, the intensity differences are not assigned to changes in gypsum content, crystallinity, nucleation, or agglomeration. The stronger reflection in C-2 is retained as an observation of the measured pattern, rather than used to explain its higher strength. The phase comparison instead rests on the characteristic reflections across the full measured range. The heat-evolution results

and XRD patterns characterize different stages of material development. Section 3.4 describes the calorimetric response within the first 480 min, whereas Figure 8 identifies the crystalline phases after 7 d. These results provide complementary information on early reaction behavior and later phase composition; the early cumulative heat differences are not directly translated into differences in hydration degree at 7 d. The XRD results establish that gypsum remained the dominant identified crystalline phase after 7 d across the investigated mixtures.

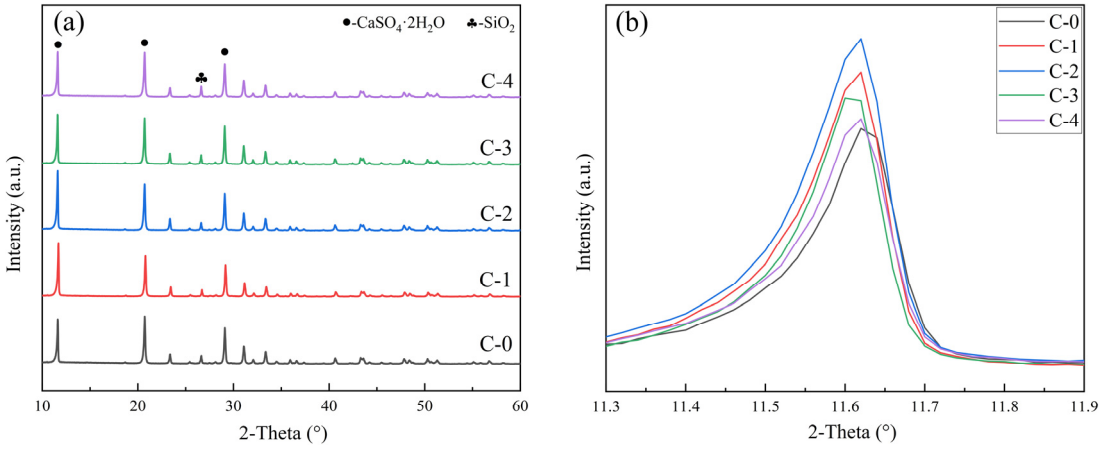


Figure 8. XRD patterns of β-HPG specimens after 7 d of curing: (**a**) full scan from 10° to 60° and (**b**) enlarged pattern in the range of 11.3–11.9°.

3.6. Effect of CSW on the Pore Structure of β-HPG

Pore structure strongly affects the mechanical strength, water absorption, and water resistance of gypsum-based materials. In this study, MIP was used to analyze the mercury-accessible porosity and equivalent pore-entry-size distribution of β-HPG specimens with different CSW dosages. The equivalent diameters describe the pore entrances or throats controlling mercury access, and the distributions are interpreted with consideration of ink-bottle and specimen-drying effects [39,40]. As shown in Figure 9a, the MIP-measured porosity of hardened β-HPG decreased continuously with increasing CSW dosage. The porosity of C-0 was 47.5%. After the incorporation of 1, 2, 3, and 4 wt% CSW, it decreased to 44.3%, 39.6%, 37.7%, and 35.0%, respectively. Compared with C-0, the corresponding reductions were 6.7%, 16.6%, 20.6%, and 26.3%. The decrease from C-0 to C-4 was therefore 12.5 percentage points, equivalent to a relative reduction of 26.3%. C-2 achieved a reduction of 7.9 percentage points, combining lower mercury-accessible porosity with the highest reported mean dry and wet strengths among the tested mixtures.

In C-0, intrusion assigned to equivalent pore-entry diameters above 1000 nm contributed 33.6 percentage points to the measured porosity of 47.5%. This corresponds to approximately 70.7% of the total intruded volume. The 200–1000 nm interval contributed 12.7 percentage points, corresponding to approximately 26.7% of the total intruded volume. In C-4, the contribution of the 200–1000 nm interval increased to 20.0 percentage points. Relative to its measured porosity of 35.0%, this represents approximately 57.1% of the total intruded volume. CSW addition therefore reduced the contribution assigned to entry diameters above 1000 nm and increased that assigned to 200–1000 nm, while the intervals below 200 nm made smaller contributions. This redistribution concerns mercury-accessible entry sizes rather than a measured conversion of individual pore bodies.

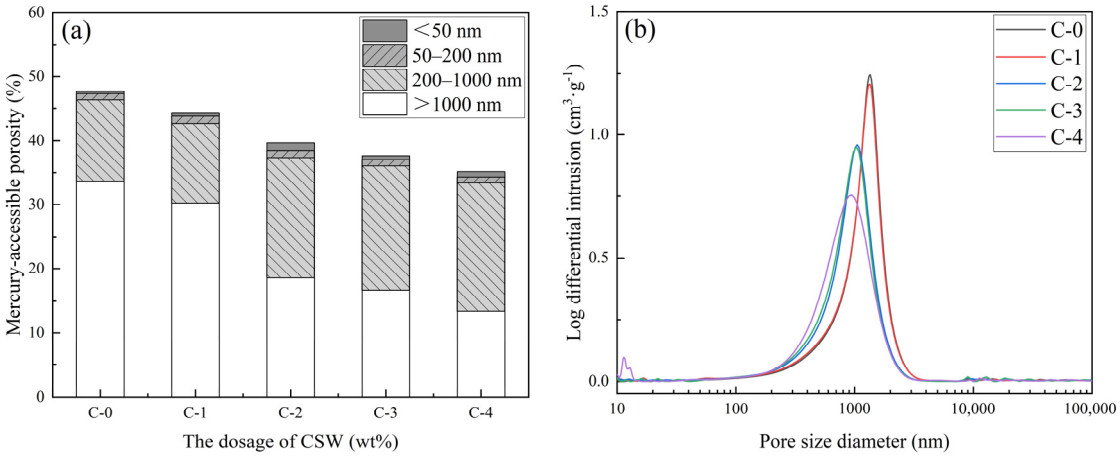


Figure 9. Effect of CSW on the pore structure of β-HPG: (**a**) total porosity and pore volume fraction in different pore size ranges and (**b**) log-differential mercury intrusion as a function of equivalent pore-entry diameter.

Figure 9b presents the corresponding differential intrusion response. The volume assigned to a size interval is assessed by integration over that interval rather than from peak height alone. The pore-structure response was obtained under the fixed W/G ratio of 0.58. With CSW added as an additional solid, the calculated initial W/S ratio decreased from 0.580 to 0.558, while paste spread also changed. Therefore, the porosity reduction is not assigned exclusively to whisker filling. C-4 exhibited the lowest measured porosity, whereas C-2 showed the highest reported mean flexural and compressive strengths. The more closely associated crystalline arrangement observed in C-2, discussed in Section 3.7, provides complementary structural context for this response. Together, these observations support considering local crystalline arrangement and fresh-paste behavior alongside accessible pore volume when selecting a formulation. The reduction in measured porosity was accompanied by a decrease in 24 h water absorption from 26.8% for C-0 to 24.3% for C-4. For C-2, the mercury-accessible porosity of 39.6% was accompanied by a water absorption of 24.9% and a mean wet compressive strength of approximately 8.5 MPa. This combination demonstrates lower water uptake and greater absolute wet load-bearing capacity relative to C-0.

3.7. Effect of CSW on the Micromorphology of β-HPG

SEM was used to compare the hardened microstructures of C-0, C-2, and C-4, representing the control mixture, the mixture with the highest mean mechanical strengths, and the highest CSW dosage, respectively. Figure 10 shows differences in crystal arrangement, visible intercrystalline voids, and localized clustering. The images were obtained from hardened and dried fragments and provide local morphological information. The comparison focuses on how crystalline features are arranged within the gypsum-dominated matrix and how these observations relate to the measured properties. As shown in Figure 10a, C-0 contained plate-like, short-prismatic, and elongated crystalline features. The exposed surface showed relatively open packing, with visible spaces between neighboring crystals. Several contacts appeared limited to crystal edges or small overlapping regions. Such an arrangement may provide fewer continuous solid connections across the observed region than a more closely interlocked structure. These features provide a morphological reference for the closer crystal associations observed in C-2 and are consistent with the higher mercury-accessible porosity of C-0. Figure 10b shows a more closely associated arrangement of plate-like and elongated features in C-2. Some elongated features appear to extend between neighboring crystalline regions, while smaller crystals occupy parts

of the surrounding spaces. The observed arrangement is consistent with improved local continuity of the hardened skeleton. Compared with C-0, this morphology also agrees with the lower mercury-accessible porosity measured by MIP. C-2 therefore combined closer local crystal associations with a reduction in measured porosity from 47.5% to 39.6%. These observations provide structural context for its approximately 49% and 23% increases in mean dry flexural and compressive strengths, respectively. Elongated features that appear to connect neighboring crystalline regions could contribute to structural continuity when adequate contact or bonding is present. The greater relative improvement in flexural strength than in compressive strength is compatible with a reinforcing contribution. The relevant morphological feature is the apparent connection between neighboring crystalline regions, rather than the presence of elongated particles alone.

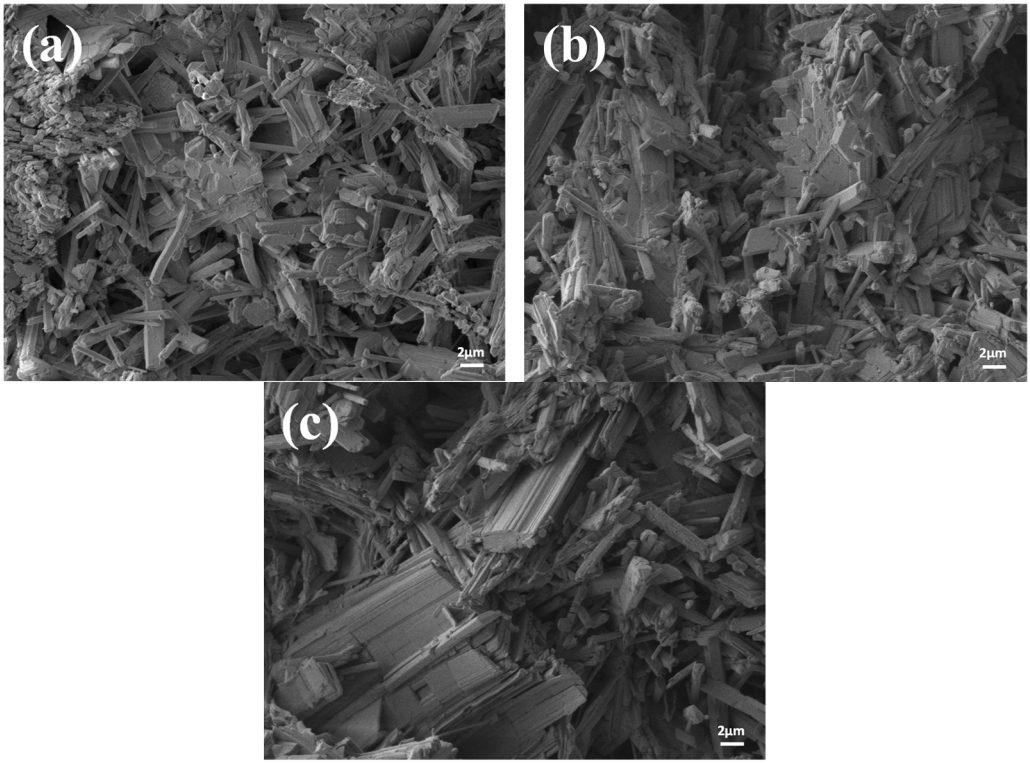


Figure 10. SEM micrographs of β-HPG specimens after curing: (**a**) C-0, (**b**) C-2, and (**c**) C-4.

The starting CSW exhibited a rod-like morphology in Figure 2b, but elongated crystals were also present in C-0, which contained no added whiskers. Previous spatially resolved studies of gypsum hydration have likewise observed the formation of needle-shaped gypsum crystals [41]. The features in C-2 may therefore include retained whiskers, newly formed gypsum crystals, or combinations of residual whiskers and associated hydration products. At 4 wt% CSW, Figure 10c shows localized bundles of relatively parallel, elongated crystalline features. These densely packed regions coexist with a less uniform surrounding arrangement. Whisker clustering, preferential gypsum crystal growth, or both may contribute to their appearance. The lower paste fluidity at this dosage may also have affected particle redistribution and the development of a uniform hardened structure. The comparison with C-2 illustrates different structural outcomes: C-4 achieved a lower mercury-accessible porosity of 35.0%, whereas C-2 combined closer crystal associations in the observed region with higher reported mean strengths. The more closely associated structure observed in C-2 also provides context for its mean wet compressive strength of approximately 8.5 MPa, compared with 7.4 MPa for C-0. The SEM comparison distinguishes relatively open packing in C-0, closer crystalline associations in C-2, and

localized bundles in C-4. These observations characterize prepared, dried specimens and complement the bulk measurements without independently identifying retained-whisker bridging or water-induced interfacial damage.

3.8. Multiscale Structure–Property Relationship and Modification Mechanism of CSW in β-HPG

The combined results highlight the mechanical benefit of CSW addition within a gypsum-dominated matrix, particularly the strength–workability combination obtained for C-2. The dry flexural and compressive strengths of C-2 reached 5.95 and 22.0 MPa, respectively, corresponding to increases of 49% and 23% relative to C-0. C-2 also exhibited the highest reported mean wet compressive strength, approximately 8.5 MPa, while retaining a paste spread diameter of 155 mm. These results provide the performance basis for examining the relationships among mixture composition, early reaction behavior, crystalline arrangement, and accessible pore structure. Figure 11 presents the proposed modification mechanism of CSW in β-HPG.

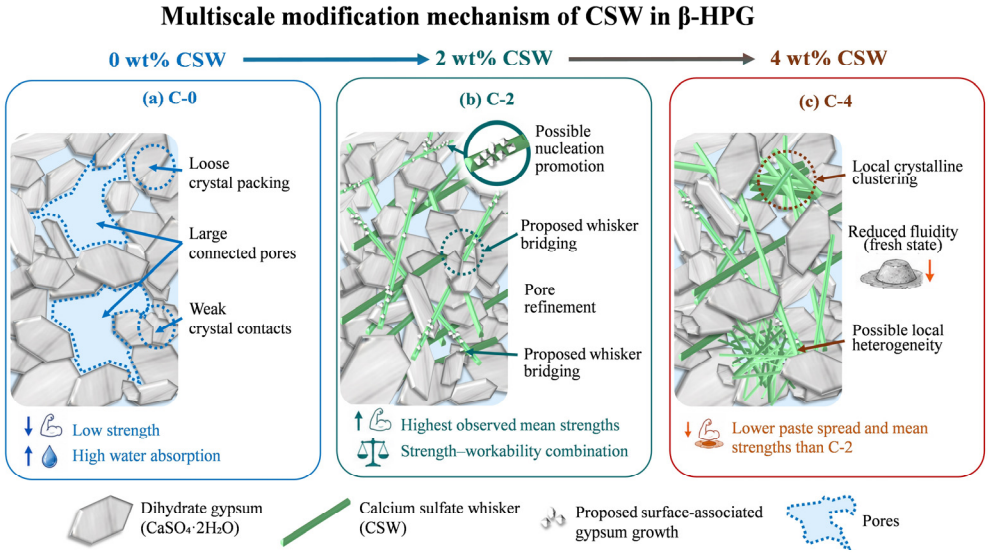


Figure 11. Proposed multiscale modification mechanism of CSW in β-HPG: (**a**) without CSW, (**b**) 2 wt % CSW, and (**c**) 4 wt % CSW.

At the fresh-paste stage, CSW reduced the fluidity and shortened the setting time of β-HPG. Similar dosage-dependent changes in setting behavior and physical properties have been reported in calcium sulfate whisker-modified gypsum composites [21,22]. In the workability and strength series, the W/G ratio was fixed at 0.58, while the calculated initial W/S ratio decreased from 0.580 to 0.558 as CSW dosage increased. The additional powder and its elongated geometry may influence particle interactions and early structural development. At 2 wt% CSW, the spread diameter remained greater than those of C-3 and C-4, providing a useful balance when considered alongside the measured strength gains. At the early hydration stage, CSW changed the hydration heat evolution of β-HPG. The main heat-flow peak shifted to an earlier time after CSW incorporation, and C-2 showed the highest heat-flow peak and cumulative heat release within 480 min. Its peak heat-flow rate of 58.46 mW/g and cumulative heat release of 103.94 J/g were approximately 18.0% and 9.83% above C-0, respectively, on the same initial-total-solid-mass basis. One possible interpretation is that the calcium sulfate surface of CSW provided additional compatible interfaces for the local precipitation and growth of $CaSO_4 \cdot 2H_2O$. This contribution is described as possible nucleation promotion.

Studies of stabilized clays relate mechanical behavior to binder type and starting mineralogy [42,43], while nanomechanical research distinguishes constituent-phase properties

from bulk composite response [44]. Research on blended cement paste also considers the role of continuing hydration in mechanical evolution [45]. These comparisons motivate evaluating reaction history, phase identity, local arrangement, and bulk strength separately in β-HPG; their specific silicate-hydrate mechanisms are not transferred to the gypsum matrix. Here, the 480 min calorimetric response and the 7 d gypsum-dominated phase assemblage describe different stages. The early heat differences are not used to determine final hydration degree, and single-peak intensities are not used to explain strength. Within the hardened matrix, C-2 showed closer crystalline associations than C-0. These local connections may contribute to load transfer and are compatible with the larger flexural-strength response, while bridging by retained CSW remains a proposed contribution.

The pore-structure results provide another link between microstructure and performance. CSW-containing formulations showed lower mercury-accessible porosity and a redistribution of intrusion volume among equivalent pore-entry-size intervals. The measured porosity decreased from 47.5% for C-0 to 35.0% for C-4. C-2 had an intermediate value of 39.6%, representing a reduction of 16.6% relative to C-0. These changes describe mercury-accessible volume and entry sizes, rather than direct conversion of individual large pore bodies into smaller pores. C-4 had the lowest MIP-measured porosity and water absorption but lower dry and wet compressive strengths than C-2. The two formulations therefore favored different measured outcomes: C-4 provided a further reduction in accessible porosity, whereas C-2 combined higher mean strengths with greater paste spread. The localized bundles observed in C-4 provide additional context for this distinction, without assigning the strength difference exclusively to CSW agglomeration. The wet-strength results further show that an appropriate amount of CSW improved the absolute load-bearing capacity of β-HPG after water exposure. The wet compressive strength increased from approximately 7.4 MPa for C-0 to 8.5 MPa for C-2. C-2 also reduced water absorption from 26.8% to 24.9%, combining approximately 14.9% higher mean wet strength with 7.1% lower water uptake. Relative strength retention represents a separate objective. The softening-coefficient point estimates were lower than those of C-0 because the proportional dry-strength increase exceeded the wet-strength increase. Thus, greater absolute capacity after immersion and a higher retained fraction of dry strength are distinct formulation outcomes. The small ratio differences among C-2, C-3, and C-4 are interpreted with consideration of uncertainty in both strength estimates, rather than used to rank specific interfacial damage mechanisms. The study by Liu et al. [46] on internal moisture evolution and humidity-dependent shrinkage in metakaolin-modified UHPC provides a useful perspective on this distinction. It examines moisture behavior together with deformation, emphasizing the importance of the moisture condition and the selected response variable. Applied to the interpretation of β-HPG, this perspective supports treating accessible pore structure, water uptake, wet strength, and moisture-induced deformation as related but different properties.

The interpretation applies to the selected β-HPG source, commercial CSW grade, and preparation conditions. The fixed-W/G series does not isolate water-ratio and consolidation effects, while the qualitative phase and morphological analyses do not quantify CSW conversion or retained-whisker load transfer. The structural observations also refer to prepared, dried specimens. Within this scope, C-2 provides a promising strength-oriented formulation. Finer dosage intervals, controlled-water comparisons, and time-resolved phase and moisture assessments would refine the proposed interpretation.

3.9. Preliminary Economic Considerations

A preliminary raw-material cost assessment was performed using indicative price ranges of CNY 370–420/t for β-building gypsum powder and CNY 4800–7000/t for CSW. The β-building gypsum price was used as a proxy for the cost of the β-HPG binder. These

ranges were treated as calculation inputs rather than verified purchase prices for the specific materials used in this study. The assessment concerns the constituent powders before water addition and does not represent the complete production or installation cost of a plaster product.

CSW was incorporated as an additional component relative to the mass of β-HPG. Therefore, the constituent cost per tonne of combined powder was calculated as:

$$C(d) = \frac{P_G + dP_{CSW}}{1 + d} \tag{4}$$

where d is the CSW-to-β-HPG mass ratio, and P_G and P_{CSW} are the respective prices in CNY/t. The relative cost increase compared with the corresponding control mixture was calculated as:

$$R_C = \frac{C(d) - P_G}{P_G} \times 100\% \tag{5}$$

Table 5 summarizes the calculated cost ranges. Both material prices were varied across their stated intervals. Each relative increase was calculated against the control cost using the same β-HPG price. At 2 wt% addition, one tonne of combined powder contained approximately 980.39 kg of β-HPG and 19.61 kg of CSW. The calculated constituent cost was CNY 456.9–549.0/t, with an increase of CNY 85.9–130.0/t relative to the corresponding control. The relative increase ranged from 20.4% to 35.1%. Thus, although the dosage was low, the cost premium was not negligible because the assumed CSW unit price was substantially higher than that of the gypsum powder. At the arithmetic midpoints of the price intervals, CNY 395/t for gypsum and CNY 5900/t for CSW, the C-2 cost was CNY 502.9/t, representing a 27.3% increase.

Table 5. Estimated constituent costs of the β-HPG–CSW powders based on the indicative price ranges.

Mixture	CSW Dosage Relative to β-HPG (wt%)	Estimated Constituent Cost (CNY/t of Combined Powder)	Relative Cost Increase Compared with C-0 (%)
C-0	0	370.0–420.0	—
C-1	1	413.9–485.1	10.3–17.7
C-2	2	456.9–549.0	20.4–35.1
C-3	3	499.0–611.7	30.4–52.2
C-4	4	540.4–673.1	40.1–68.9

The value of this additional expenditure depends on the performance requirement. C-2 showed reported mean dry flexural and compressive strength increases of approximately 48.8% and 22.9%, respectively. Its wet compressive strength increased by approximately 14.9%, based on the reported values of 7.4 and 8.5 MPa. To compare these different benefits, a relative strength-to-material-cost indicator was calculated:

$$I_s = \frac{f_{s,2}/f_{s,0}}{C_2/C_0} \tag{6}$$

where $f_{s,2}$ and $f_{s,0}$ are the reported mean values of the selected strength property for C-2 and C-0. Values above 1 indicate an improved strength-to-material-cost ratio on the selected powder-mass basis.

As shown in Table 6, the dry flexural-strength-to-material-cost indicator exceeded 1 throughout the assumed price range, whereas the dry compressive-strength indicator depended on the price combination and the wet-strength indicator remained below 1. The cost premium is therefore most relevant where dry flexural performance is a specified requirement. This assessment covers powder costs only; verified procurement, production,

and application costs are needed for a product-level decision. C-2 uses less CSW than C-3 and C-4 while providing higher mean strengths, but a lower dosage may be preferable when it already meets the required performance.

Table 6. Relative strength-to-material-cost indicators for C-2 over the assumed price intervals.

Selected Property	Reported Mean Strength Ratio, C-2/C-0	Relative Strength-to-Material-Cost Indicator, I_s
Dry flexural strength	1.488	1.10–1.23
Dry compressive strength	1.229	0.91–1.02
Wet compressive strength	1.149	0.85–0.95

4. Conclusions

This study investigated the dosage-dependent effects of calcium sulfate whisker (CSW) on the performance and microstructure of β-hemihydrate phosphogypsum (β-HPG). The main conclusions are as follows.

(1) Among the five formulations tested at W/G = 0.58, C-2 achieved the highest mean dry flexural and compressive strengths of 5.95 and 22.0 MPa, respectively, approximately 49% and 23% above C-0. Although CSW addition reduced paste spread and shortened setting times, C-2 retained a spread diameter of 155 mm, compared with 138 and 110 mm for C-3 and C-4. This combination identifies 2 wt% CSW as a promising tested dosage for balancing strength and workability.

(2) C-2 increased the mean wet compressive strength after 24 h immersion from 7.4 to approximately 8.5 MPa and reduced water absorption from 26.8% to 24.9%. Its mechanical benefit therefore extended to the tested immersion condition. The softening-coefficient point estimates nevertheless remained below that of C-0, distinguishing greater absolute wet load-bearing capacity from improved relative strength retention. Small differences among the higher-dosage formulations require consideration of uncertainty in both dry and wet strengths.

(3) Mercury-accessible porosity decreased from 47.5% to 35.0% as CSW dosage increased from 0 to 4 wt%, accompanied by a redistribution of intrusion volume among equivalent pore-entry-size intervals. C-2 exhibited a porosity of 39.6% and more closely associated crystalline regions in SEM observations, whereas C-4 showed localized bundle-like arrangements. The highest mean strengths and the lowest accessible porosity occurred in different formulations, demonstrating the importance of considering local crystalline arrangement and workability alongside pore-volume reduction.

(4) CSW-containing pastes reached their main exothermic peaks earlier than C-0. C-2 exhibited the highest recorded peak of 58.46 mW/g and cumulative heat of 103.94 J/g within 480 min, approximately 18.0% and 9.83% above C-0 on the initial-total-solid-mass basis. Gypsum remained the dominant identified crystalline phase after 7 d. These results distinguish early calorimetric response from later phase identity; possible nucleation promotion, CSW reaction, and retained-whisker bridging remain proposed contributions.

The study distinguishes the formulation with the highest mean strengths from that with the lowest accessible porosity and separates absolute wet capacity from relative strength retention. These relationships support performance-targeted formulation design. Finer dosage intervals, constant-W/S or matched-spread comparisons, and phase-resolved and longer-term moisture assessments would further refine the formulation and proposed mechanisms.

Author Contributions: Conceptualization, H.Z. and D.L.; methodology, J.J.; software, H.Z.; validation, T.L.; formal analysis, Z.Z.; investigation, Y.X.; resources, H.Z.; data curation, S.C.; writing—original draft preparation, H.Z. and S.C.; writing—review and editing, H.Z. and D.L.; visualization, S.C.; supervision, H.Z. and D.L.; project administration, H.Z.; funding acquisition, H.Z. All authors have read and agreed to the published version of the manuscript.

Funding: This study was funded by the Jiangsu Marine Structure Service Performance Improvement Engineering Research Center (Grant No. CP12015005), Jiangsu University Key (Construction) Laboratory of Offshore Floating Wind Power Technology and Equipment and the University-level Fund of Nantong Institute of Technology (Project number: 2024XK(Z)07 and 2024XK (Z)08).

Data Availability Statement: The data presented in this study are available on request from the corresponding author.

Conflicts of Interest: The authors declare no conflicts of interest.

References

1. Dunant, C.F.; Joseph, S.; Prajapati, R.; Allwood, J.M. Electric recycling of Portland cement at scale. *Nature* **2024**, *629*, 1055–1061. [CrossRef] [PubMed]
2. Zhang, X.; Zhao, H.; Tao, Z.; Li, W. Performance of sustainable cementitious mortar incorporating hybrid waste glass powder and steel slag. *Constr. Build. Mater.* **2025**, *472*, 140928. [CrossRef]
3. Nader, M.A.; El-Hariri, M.O.R.; Kamar, A.; Fathy, I.N.; Saif, M.S. Experimental and numerical evaluation of the mechanical behavior of alkali-activated slag concrete with recycled waste glass and dealuminated metakaolin powders. *Sci. Rep.* **2026**, *16*, 6364. [CrossRef] [PubMed]
4. Bouzeriba, H.; Bouzidi, N.; Idres, A.; Laala, I.; Merzeg, F.A. Iron mining waste as a sustainable material for producing bricks: Microstructure, mechanical and thermal properties. *Clay Miner.* **2025**, *60*, 273–284. [CrossRef]
5. Li, X.; Bai, T.; Liu, T.; Umar, H.A.; Hu, X.; Shi, C. Effects of low pressure and low humidity on hydration and freeze-thaw resistance of air-entrained concrete with fly ash and GGBS. *Cem. Concr. Compos.* **2026**, *170*, 106566. [CrossRef]
6. Kamarou, M.; Moskovskikh, D.; Kuskov, K.; Yudin, S.; Akinwande, A.A.; Smorokov, A.; Özkılıç, Y.O.; Abdulwahid, M.Y.; Bhowmik, A.; Romanovskaia, E.; et al. High-strength gypsum binder with improved water-resistance coefficient derived from industrial wastes. *Waste Manag. Res.* **2025**, *43*, 213–224. [CrossRef] [PubMed]
7. Cao, W.; Yi, W.; Peng, J.; Li, J.; Yin, S. Recycling of phosphogypsum to prepare gypsum plaster: Effect of calcination temperature. *J. Build. Eng.* **2022**, *45*, 103511. [CrossRef]
8. Zhang, L.; Mo, K.H.; Tan, T.H.; Hung, C.-C.; Yap, S.P.; Ling, T.-C. Influence of calcination and GGBS addition in preparing β-hemihydrate synthetic gypsum from phosphogypsum. *Case Stud. Constr. Mater.* **2023**, *19*, e02259. [CrossRef]
9. Jin, Z.; Ma, B.; Su, Y.; Qi, H.; Lu, W.; Zhang, T. Preparation of eco-friendly lightweight gypsum: Use of beta-hemihydrate phosphogypsum and expanded polystyrene particles. *Constr. Build. Mater.* **2021**, *297*, 123837. [CrossRef]
10. Huang, W.; Tan, Y.; Ming, H.; Li, H.; Wu, J.; Wu, C.; Hu, B. A novel method for preparing phosphorus building gypsum (PBG)-based building materials with low water/gypsum ratios. *J. Mater. Cycles Waste Manag.* **2023**, *25*, 1035–1049. [CrossRef]
11. Chen, X.; Liu, Y.; Wu, Q.; Ding, Y.; Wang, Q.; Tang, W.; Zhu, B. Study on physical and chemical characteristics of β-hemihydrate phosphogypsum. *Case Stud. Constr. Mater.* **2022**, *17*, e01461. [CrossRef]
12. Yu, Q.L.; Brouwers, H.J.H. Microstructure and mechanical properties of β-hemihydrate produced gypsum: An insight from its hydration process. *Constr. Build. Mater.* **2011**, *25*, 3149–3157. [CrossRef]
13. Jia, R.; Wang, Q.; Feng, P. A comprehensive overview of fibre-reinforced gypsum-based composites (FRGCs) in the construction field. *Compos. Part B Eng.* **2021**, *205*, 108540. [CrossRef]
14. Garg, M.; Pundir, A.; Singh, R. Modifications in water resistance and engineering properties of β-calcium sulphate hemihydrate plaster-superplasticizer blends. *Mater. Struct.* **2016**, *49*, 3253–3263. [CrossRef]
15. Wang, L.; Cao, M.; Li, X.; Du, W.; Wang, X. A novel approach for improving the water resistance of gypsum plaster by internal mixing hypromellose and external coating waterproofing agent. *Constr. Build. Mater.* **2023**, *401*, 132940. [CrossRef]
16. Zhu, C.; Zhang, J.; Peng, J.; Cao, W.; Liu, J. Physical and mechanical properties of gypsum-based composites reinforced with PVA and PP fibers. *Constr. Build. Mater.* **2018**, *163*, 695–705. [CrossRef]
17. Suárez, F.; Felipe-Sesé, L.; Díaz, F.; Gálvez, J.; Alberti, M. On the fracture behaviour of fibre-reinforced gypsum using micro and macro polymer fibres. *Constr. Build. Mater.* **2020**, *244*, 118347. [CrossRef]
18. Gonçalves, R.; Martinho, A.; Oliveira, J. Evaluating the potential use of recycled glass fibers for the development of gypsum-based composites. *Constr. Build. Mater.* **2022**, *321*, 126320. [CrossRef]

19. Zheng, M.; Zhang, Y.; Chen, Z.; Wu, Z.; Li, K.; Liao, C.; Pu, Y.; Zaheer, A. Static and cyclic hydro-mechanical performance of cement stone reinforced with fiber carrier-encapsulated MICP. *Acta Geotech.* **2026**, 1–35. [CrossRef]
20. Zhang, L.; Mo, K.H.; Tan, T.H.; Yap, S.P.; Lee, F.W.; Ling, T.-C. Synthesis and characterization of fiber-reinforced lightweight foamed phosphogypsum-based composite. *Constr. Build. Mater.* **2023**, *394*, 132244. [CrossRef]
21. Wang, D.; Chen, C.; Wang, Y.; Jiu, S.; Chen, Y. Influence of modified calcium sulfate hemihydrate whisker on the physical, mechanical, and microscopic properties of gypsum matrix composites. *Constr. Build. Mater.* **2023**, *394*, 132280. [CrossRef]
22. Jian, S.; Yang, X.; Gao, W.; Li, B.; Gao, X.; Huang, W.; Tan, H.; Lei, Y. Study on performance and function mechanisms of whisker modified flue gas desulfurization (FGD) gypsum. *Constr. Build. Mater.* **2021**, *301*, 124341. [CrossRef]
23. Cao, K.; Liu, G.; Li, H.; Huang, Z. Mechanical properties and microstructure of calcium sulfate whisker-reinforced cement-based composites. *Materials* **2022**, *15*, 947. [CrossRef] [PubMed]
24. Aakriti; Maiti, S.; Jain, N.; Prajapati, P. Synthesis of calcium sulfate whiskers via acidification exploiting FGD gypsum for improved binder properties. *Sustain. Chem. Pharm.* **2024**, *42*, 101745. [CrossRef]
25. Wang, X.; Jin, B.; Fan, M.; Liu, X.; Zhang, X.; Zhang, J.; Li, S.; Zhang, W. A feasible route for preparation of calcium sulfate whiskers from FGD gypsum via filtrate recycle under hydro-thermal conditions. *Processes* **2023**, *11*, 1809. [CrossRef]
26. Jiao, J.; Shen, X.; Ding, H.; Lu, D.; Li, D. Study on the hydration and properties of multiphase phosphogypsum synergistically activated by sodium sulfate and calcium sulfate whisker. *Constr. Build. Mater.* **2022**, *355*, 129225. [CrossRef]
27. Wang, Y.; Song, J.; Hu, Z.; Zhang, Y.; Guan, Z.; Yang, H. Mechanical and water resistance properties of strain hardening fiber reinforced gypsum-based composites. *Constr. Build. Mater.* **2024**, *425*, 136116. [CrossRef]
28. Schmid, T.; Jungnickel, R.; Dariz, P. Insights into the $CaSO_4$–H_2O System: A Raman-Spectroscopic Study. *Minerals* **2020**, *10*, 115. [CrossRef]
29. Singh, N.B. The Activation Effect of K_2SO_4 on the Hydration of Gypsum Anhydrite, $CaSO_4$(II). *J. Am. Ceram. Soc.* **2005**, *88*, 196–201. [CrossRef]
30. *GB/T 9776-2008*; Calcined Gypsum. Standards Press of China: Beijing, China, 2008.
31. *GB/T 17669.4-1999*; Gypsum Plasters—Determination of Physical Properties of Pure Paste. Standards Press of China: Beijing, China, 1999.
32. Lewry, A.J.; Williamson, J. The setting of gypsum plaster: Part II The development of microstructure and strength. *J. Mater. Sci.* **1994**, *29*, 5524–5528.
33. Zhu, Z.; Wang, J.; Wu, Q.; Zhu, H.; Wang, M.; Yang, T. Molecular dynamics simulation of water resistance enhancement of gypsum modified by polymethylhydrosiloxane (PMHS). *Constr. Build. Mater.* **2024**, *435*, 136801. [CrossRef]
34. Fobbe, N.; Goetz-Neunhoeffer, F.; Jansen, D. The influence of calcium formate on the hydration of calcium sulfate hemihydrate. *Mater. Struct.* **2023**, *56*, 92. [CrossRef]
35. Gurgul, S.J.; Seng, G.; Williams, G.R. A kinetic and mechanistic study into the transformation of calcium sulfate hemihydrate to dihydrate. *J. Synchrotron Radiat.* **2019**, *26*, 774–784. [CrossRef] [PubMed]
36. Heeb, J.; Healy, D.; Timms, N.E.; Gomez-Rivas, E. Rapid hydration and weakening of anhydrite under stress: Implications for natural hydration in the Earth's crust and mantle. *Solid Earth* **2023**, *14*, 985–1003. [CrossRef]
37. Inoue, M.; Hirasawa, I. The relationship between crystal morphology and XRD peak intensity on $CaSO_4{\cdot}2H_2O$. *J. Cryst. Growth* **2013**, *380*, 169–175. [CrossRef]
38. McCusker, L.B.; Von Dreele, R.B.; Cox, D.E.; Louër, D.; Scardi, P. Rietveld refinement guidelines. *J. Appl. Crystallogr.* **1999**, *32*, 36–50. [CrossRef]
39. Zhang, Y.; Wu, K.; Yang, Z.; Ye, G. A reappraisal of the ink-bottle effect and pore structure of cementitious materials using intrusion-extrusion cyclic mercury porosimetry. *Cem. Concr. Res.* **2022**, *161*, 106942. [CrossRef]
40. Gallé, C. Effect of drying on cement-based materials pore structure as identified by mercury intrusion porosimetry: A comparative study between oven-, vacuum-, and freeze-drying. *Cem. Concr. Res.* **2001**, *31*, 1467–1477. [CrossRef]
41. La Bella, M.; Besselink, R.; Wright, J.P.; Van Driessche, A.E.; Fernandez-Martinez, A.; Giacobbe, C. Hierarchical synchrotron diffraction and imaging study of the calcium sulfate hemihydrate–gypsum transformation. *J. Appl. Crystallogr.* **2023**, *56*, 660–672. [CrossRef] [PubMed]
42. Su, Y.; Luo, B.; Luo, Z.; Xu, F.; Huang, H.; Long, Z.; Shen, C. Mechanical characteristics and solidification mechanism of slag/fly ash-based geopolymer and cement solidified organic clay: A comparative study. *J. Build. Eng.* **2023**, *71*, 106459. [CrossRef]
43. Luo, B.; Su, Y.; Hu, X.; Chen, Z.; Chen, Y.; Ding, X. Strength behavior and microscopic mechanisms of geopolymer-stabilized waste clays considering clay mineralogy. *J. Clean. Prod.* **2025**, *530*, 146877. [CrossRef]
44. Wang, J.; McElhany, S.; Hu, Z.; Liu, J.; Carraro, C.; Monteiro, P.J.; Maboudian, R. Critical review of nanomechanical properties of calcium (alumino) silicate hydrates: Test methods, influencing factors, and enhancing strategies. *Engineering* **2026**, *in press*. [CrossRef]

45. Wang, J.; Zhu, X.; Wang, J.; Chen, Y.; Liu, Y.; Hu, Z.; Liu, J.; Maboudian, R.; Monteiro, P.J.M. Does the hydration process of supplementary cementitious materials affect the aging creep of blended cement paste? *Cem. Concr. Res.* **2025**, *191*, 107826. [CrossRef]
46. Liu, Z.; Dong, T.; Lv, Y.; Qi, X.; Shui, Z. Internal moisture evolution and humidity-dependent shrinkage behavior of metakaolin-modified ultra-high-performance concrete. *Constr. Build. Mater.* **2026**, *541*, 147873. [CrossRef]

Disclaimer/Publisher's Note: The statements, opinions and data contained in all publications are solely those of the individual author(s) and contributor(s) and not of MDPI and/or the editor(s). MDPI and/or the editor(s) disclaim responsibility for any injury to people or property resulting from any ideas, methods, instructions or products referred to in the content.